ISSN (Print) 1226-1750
ISSN (Online) 2233-6656
Journal of Magnetics 30(4), 565-574 (2025) https://doi.org/10.4283/JMAG.2025.30.4.565

Configurational Effects in Ferromagnetic Resonance Spectra of Clusters of Macrospins

Wonbae Bang[1]*, M. B. Jungfleisch[2], J. B. Ketterson[3], and F. Montoncello[4]*

[1]*School of Liberal Arts, Korea University of Technology and Education, Cheonan 31253, Republic of Korea*
[2]*Department of Physics and Astronomy, University of Delaware, Newark, DE 19716, USA*
[3]*Department of Physics and Astronomy, Northwestern University, Evanston, IL 60208, USA*
[4]*Dipartimento di Fisica e Scienze della Terra, Università di Ferrara, Ferrara, I-44121, Italy*

(Received 28 February 2025, Received in final form 23 September 2025, Accepted 24 September 2025)

We present experimental and theoretical investigations of spin wave modes in Permalloy ($Ni_{80}Fe_{20}$) macrospin arrays in cross and square configurations to understand the dynamics among clusters of them. These configurations are periodically patterned at the central signal line of a coplanar waveguide to acquire strong coupling with the microwave field. Their dynamic behavior is analyzed using broadband ferromagnetic resonance (FMR) measurements. Our results reveal a notable mode-splitting associated with a rotation of the macrospin configuration, highlighting the influence of the geometry on spin wave excitations. Furthermore, the spectra depend on the macrospin configuration as evidenced by the discontinuity of the FMR curves associated with different magnetization reversal fields, and the interaction between modes at low frequency. Theoretical calculations support the experimental observations of fundamental modes and mode-splitting at the vertex region. These findings contribute to the development of artificial spin ice (ASI) for functional magnonic networks and spin-based computing applications.

Keywords : artificial spin ice, spin wave mode, ferromagnetic resonance

1. Introduction

Artificial spin ice (ASI) systems have emerged as a versatile platform for exploring spin dynamics [1-4], offering new opportunities for advancements in magnonics [5], reconfigurable computing [6], and high-density data storage [7]. These engineered lattices, composed of interacting nano-magnetic elements, exhibit rich collective behaviors, including spin wave excitations and the formation of topological magnetic defects [8]. A key feature of ASI is geometric frustration, which arises from competing dipolar interactions, leading to a highly degenerate energy landscape that supports diverse magnetic states [9-13]. This intrinsic complexity not only provides an opportunity to investigate fundamental magnetization dynamics but also paves the way for energy-efficient spintronic applications, such as wave-based logic, unconventional computing paradigms, and neuromorphic computing applications [14].

A main focus of ASI studies is the impact of lattice geometry and vertex configurations on magnetic ground states and spin wave excitation spectra. Different ASI systems, such as kagome, square, and honeycomb lattices, have been widely investigated [15-17], including the effects of a regular distortion of the lattice geometry itself [11, 12], demonstrating that the spatial arrangement of the nano-elements critically determines dipolar interactions and spin wave propagation.

Here, we report the effects of configuration variations on ferromagnetic resonance (FMR) spectra of macrospin arrays of four dipolarly coupled elements in the different orientations. In order to experimentally probe the spin wave dynamics, we nanoengineered devices which consist of macrospin arrays patterned on coplanar waveguides which yield maximal intensity of the FMR spectra when measured with a vector network analyzer. Our experimental FMR measurements were compared to micromagnetic simulations. Experiments and calculations

*Co-corresponding author: Tel: +82-41-560-1110,
E-mail: wbang@koreatech.ac.kr
Tel: +39-0532-974249,
E-mail: montoncello@fe.infn.it

show that the complex behavior of macrospins can be understood from the intrinsic properties of their individual building blocks consisting of more than just one element, but a cluster of four [18].

2. Experimental Setup and Theoretical Calculation

Our devices consist of a 50 Ω matched coplanar waveguides (CPW) with Permalloy (Py, $Ni_{80}Fe_{20}$) macrospin arrays patterned on the central signal line. Fig. 1(a) shows an array of four macrospins configured as a cross (Type I in Fig. 1(b)) on a Si substrate with 300 nm of SiO_2. The CPW consists of an electron-beam deposited 100 nm Au layer on top of a 5 nm Ti layer patterned photolithographically with a laser writer followed by a lift-off process. The permalloy macrospin arrays are patterned directly on top of the central signal line of the CPW using electron-beam lithography from a 15 nm electron-beam deposited film followed by a lift-off. The deposition rates, as monitored by a quartz crystal microbalance, were ~0.2 Å/sec for Ti, 1.4 Å/sec for Au, and 0.4 Å/sec for permalloy with 3×10^{-7} Torr base pressure during all evaporations [19].

We fabricated four different types of macrospin configurations (Type I: cross, Type II: square, Type III: 45° rotated cross, and Type IV: 45° rotated square) on separate CPWs to study the effect of an interaction between macrospins, as shown in Fig. 1(b). Since the distance between macrospin configurations in the array is 2 μm, interactions between the configurations can be ignored. In Fig. 1(b), the major axis of the "macrospin 1" is parallel to the applied magnetic field; however, the major axis of "macrospin 2" is perpendicular to the field. The major axes of the macrospins 3 and 4 in Fig. 1(b) are 45° and 135° from the applied field, respectively. SEM images of each macrospin of the four different types of configurations indicate that they are 500 nm long and 200 nm wide and ellipse-like in shape, as shown in Fig. 2.

Broadband ferromagnetic resonance (FMR) measurements were conducted to analyze the spin wave modes of the arrays using a vector network analyzer (VNA), which was connected to the CPW to record the microwave absorption spectra, with the transmission parameter S_{21} measured at a nominal microwave power of 0 dBm. All spectra were recorded using the following procedures: first the macrospins were magnetized at +3000 Oe, and the frequency was swept from 2 to 10 GHz to establish a

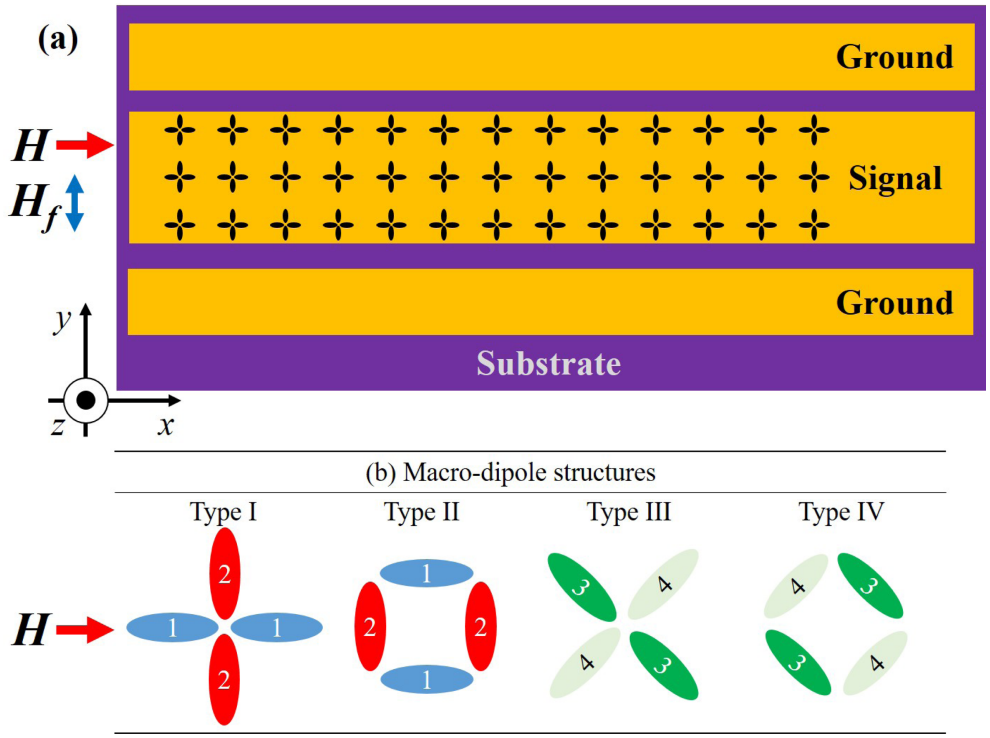

Fig. 1. (Color online) (a) Schematic of measurement setup of the macrospin arrays on the coplanar waveguide for the Type I (cross) array. The 15 nm of permalloy macrospin arrays directly fabricated on top of the central signal line. The direction of the applied magnetic field is parallel to the coplanar waveguide axis. Since the center-to-center in the array is 2 μm, interactions between neighboring configurations are ignored. (b) Four different types of the macrospin arrays studied in the experiments and simulations.

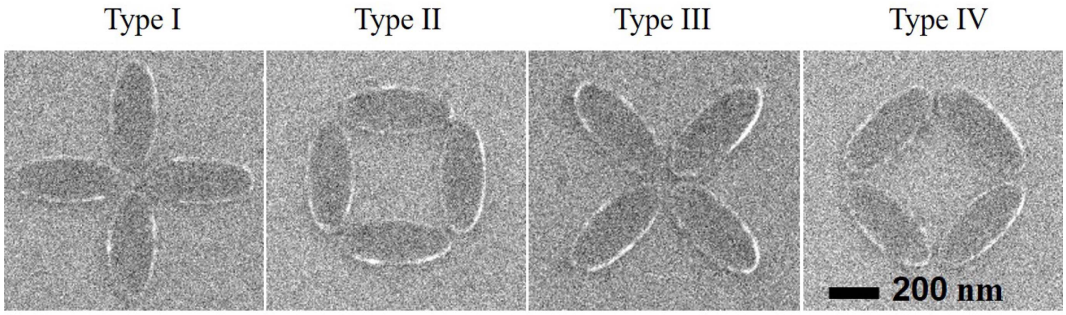

Fig. 2. SEM images of the four different types of the configurations: (a) cross, (b) square, (c) 45° rotated cross, and (d) 45° rotated square. Each of the configurations is written on a different coplanar waveguide. Each macrospin dimension is 500 nm × 200 nm, while the thickness is 15 nm.

baseline, which was then subtracted from subsequent measurements at all other fields. The frequency was then swept in a range of 2-10 GHz for applied fields from +900 Oe to –900 Oe in 10 Oe steps.

We performed micromagnetic simulations with the GPU-accelerated program Mumax3 [20]. We discretized the four arrays (Type I-IV) through elemental square cells with dimension $5 \times 5 \times 15$ nm^3. Each macrospin had an elliptical shape of $500 \times 200 \times 15$ nm^3. The minimum distance between adjacent macrospins (whose long axes are perpendicular to each other) was set to about 28 nm (considering on a square mesh the oblique edge-to-edge distance). The magnetic parameters are: saturation magnetization M_s=650 Oe, exchange stiffness constant A=10.0 pJ/m, gyromagnetic ratio γ=18.5 rad GHz/kOe (typical of Permalloy).

We also considered a slight tilt of 2 degrees between the applied field and the axes of the macrospins to meet experimental conditions and to break the symmetry to avoid artifacts in the simulations.

We excite the system with a sinc (i.e., cardinal sine) microwave field:

$$b(t) = b_0 \frac{\sin(2\pi f_0(t-t_0))}{2\pi f_0(t-t_0)} \tag{1}$$

with time delay $t_0 = 2$ ns, cutoff frequency $f_0 = 20$ GHz and amplitude $b_0 = 10$ Oe. We recorded the magnetization distribution every 20 ps, which sets the maximum frequency to 20 GHz (Nyquist frequency), and for a total time of 50 ns, which sets the frequency resolution to 0.02 GHz. At each field step of 10 Oe, from 900 Oe to -900 Oe, we performed the space-time Fourier transform, and obtained the frequency spectrum of the system, as well as the dynamic magnetization profiles (spin wave modes), as a function of the applied field.

In the following, for the mode phase profiles we plot the real part of the out-of-plane (z) component of the dynamic magnetization $\delta m_z(x, y, H)$, while for the frequency/field curves, to be compared with the FMR spectra, we plot the square modulus of the integral of $m_z(x, y, H)$ over the primitive cell area S at each applied field H:

$$I(H) = \left| \iint_S \delta m_z(x, y, H) dx dy \right|^2 . \tag{2}$$

3. Results and Discussion

In Fig. 3, we show a comparison between the experimentally measured and theoretically simulated FMR frequency-field curves for Type I and II samples. The white arrows in the panels indicate the correspondence of a few subtle details between measurement and simulation. In particular, simulations show three main modes with significant intensity, likely to be detected in the experiments: an edge mode and the two fundamental modes localized in macrospins either perpendicular or parallel to the applied field (see Fig. 4(a-c) for Type I and (d-f) for Type II).

First, we discuss the fundamental mode $F_{||}$ (Fig. 4-c) localized in the macrospins parallel to the applied field, which has the highest frequency (lowest demagnetizing field). We superimposed the analytical (dotted) curve of the modified Kittel FMR expression in Fig. 3 (panel (c) only):

$$f = \frac{\gamma}{2\pi} \mu_0 \sqrt{(H_0 + H_A)[(H_0 + H_A) + M_S]} \tag{3}$$

where $\mu_0 = 4\pi \times 10^{-7}$ H/m, H_0 is the applied field, and $H_A = 360$ Oe is an effective anisotropy field introduced in the formula to account for a reversal (of the macrospins parallel to the field and aligned along their major axis of Type I) occurring at –360 Oe (while in the uniformly magnetized film it would be zero). In this way, we show

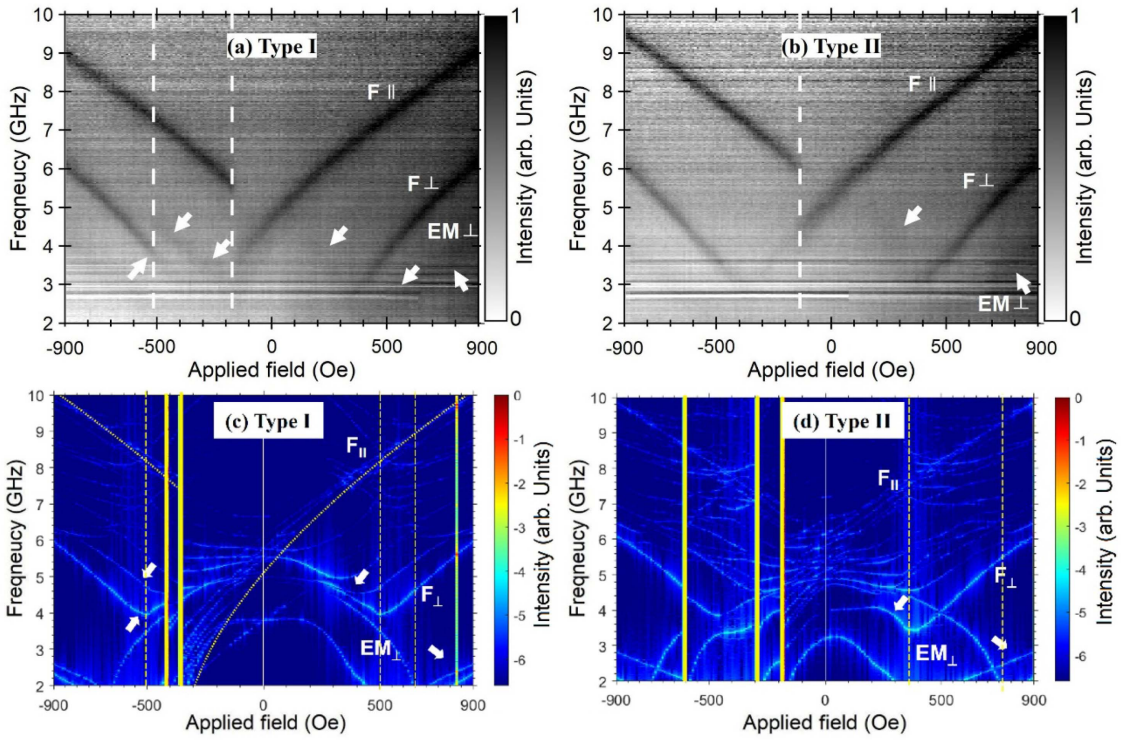

Fig. 3. (Color online) The experimental FMR spectra (top (a) and (b)) compared with theoretical simulations (bottom (c) and (d)) for Type I and Type II macrospin arrays. In the simulations, the vertical bold lines mark the discontinuous transitions, while the dashed lines mark the continuous transitions. From the right to the left: H_1 is 650 Oe for Type I, 750 Oe for Type II; H_2=500 Oe for Type I and 400 Oe for Type II, H_3 is -360 Oe in Type I and -190 Oe in Type II; H_4 is -420 Oe in Type I and -300 Oe in Type II; H_5 is -500 Oe in Type I and -620 Oe in Type II. The dotted line in panel (c) is the analytical curve of the Kittel mode, adapted to include an anisotropy field H_A=360 Oe (found in the simulations), which accounts for the elliptical shape of the macrospins: this line mostly overlaps with the simulated curve of the mode localized in the macrospins aligned with the applied field. The labels indicate the fundamental (F) and the edge (EM) modes localized in macrospins parallel (||) or perpendicular (⊥) to the applied field. The white arrows indicate subtle effects found in the experiment with a corresponding signature in the simulation. All color bars are in arbitrary units.

how the magnetic dipole moment density and their alignment with the applied field govern the dynamics of the fundamental mode (independently of the edge details).

Moreover, in Fig. 3 we identify the fundamental mode $F_\perp$ (see Fig. 4-b for the simulated profile) and, with a considerably smaller intensity, the edge mode $EM_\perp$ (see Fig. 4-a for the simulated profile, $EM_\perp$ is indicated with a white arrow in Fig. 3), which occur only in macrospins perpendicular to the applied field, the former localized in the main central part of the macrospin, the second at the edges along the direction of the applied field.

Type I and II (as well as III and IV) can be considered equivalent, having two macrospins parallel ("macrospin 1" in Fig. 1-b) and the others perpendicular ("macrospin 2") to the applied field, except for the different symmetry of the macrospin interactions: central in Type I (III), distributed to the four corners in Type II (IV). This discrepancy plays almost no role in the experiment (where bulk fundamental modes primarily contribute to the signal, not the edge modes), while it is rather important in the simulations (where edge modes are also visible). The more pronounced contribution of edges in the simulations might be due to an underestimation of the assumed theoretical macrospin-macrospin distance due to the difficulty modeling the exact experimental conditions such as shape and shape distribution across the lattice.

We now analyze and interpret the spectra of the Type I and II samples separately. Looking to the FMR spectrum of Type I, we identify five transition points, which can be understood with reference to the simulated ground state magnetization distributions, as shown in Fig. 5. Starting from H = +900 Oe, at high field values the magnetization in either macrospin 1 and 2 is saturated and is not changing its configuration (i.e., the magnetic moment space distribution remains the same). Hence, the frequency/field behavior is almost linear (Larmor-like): $\omega = \gamma\mu_0 H$.

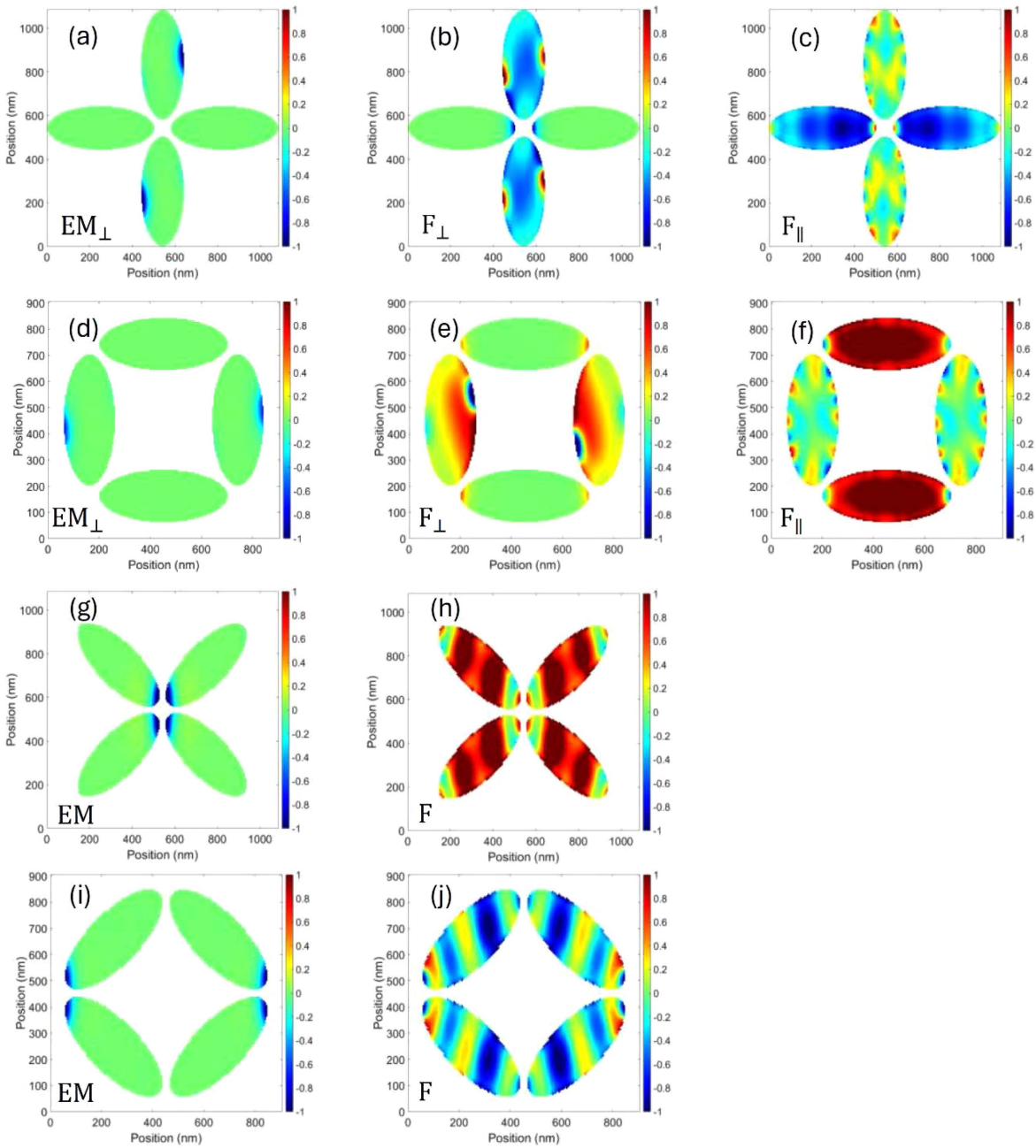

Fig. 4. (Color online) Profiles (real part of the out-of-plane component of the dynamic magnetization) of the spin wave modes calculated at H=900 Oe for (a-c) Type I; (d-f) Type II; (g), (h) Type III; (i), (j) Type IV macrospin system. Labels, associated to each panel, are discussed in the text, and indicate either the fundamental (F) or the edge (EM) mode localized in macrospins parallel (||) or perpendicular (⊥) to the applied field when not degenerate in frequency. The occasional undulation of the profiles indicates a light hybridization of the fundamental modes with higher order modes with a backward character [22].

In reducing the applied field, the shape anisotropy of "macrospin 2" (perpendicular to H) becomes progressively dominant, causing a continuous (but not uniform) rotation of the magnetic moments from the hard to the easy axis of "macrospin 2". At around H_1, i.e., 650 Oe (Type I) or 750 Oe (Type II), only edge magnetic moments are involved, but at around H_2, i.e., 500 Oe (Type I) or 400 Oe (Type II) bulk magnetic moments start to be relevant. While the applied field is decreasing, the gradual rotation of "macrospin 2" magnetization towards its easy axis favors a progressively increased system stability, i.e., smaller demagnetizing fields and a stiffer magnetization in

"macrospin 2", and hence a progressively higher frequency of mode $F_\perp$ and $EM_\perp$ until H=0. The white arrows in Fig. 3 show the correspondence between measurements and simulations relative to the weak FMR signal, in narrow field ranges, coming from modes such as $F_\perp$ and $EM_\perp$. In contrast, shape anisotropy of "macrospin 1", favors a magnetization parallel to the applied field and is invariant even when the field polarity changes at H=0. Hence, the corresponding mode favors a linear frequency behavior, gradually turning to a square root behavior below H=0 (see Eq. 1).

In the Type I spectra, the strong discontinuity in the FMR curves at $H_3 = -360$ Oe (around –180 Oe in the measured spectra) is due to the magnetization reversal of the macrospins parallel to the applied field: in fact, the frequency difference in the spectrum is around 3 GHz. At $H_4 = -420$ Oe, another discontinuity appears in the FMR spectrum, which is due to the formation of a characteristic C-state magnetization [21] in the macrospins perpendicular to the applied field (see Fig. 5, H = –420 Oe, for the corresponding magnetization map): despite this transition being subtle (and gradual), and the field interval within which it occurs is limited, we can recognize its signature in the measured spectra between –200 Oe and –500 Oe (signaled by two white arrows in Fig. 3-(a), (c)), where two parallel curve branches can be seen, the upper one fading as the field is increased in the negative direction. The last transition occurs at $H_5 = -500$ Oe (–510 Oe in the experiments) where the magnetization configuration switches from a C-state to the mirror of the equivalent one at positive field values: in the simulations, this transition field (–500 Oe) corresponds to a minimum in the frequency of $F_\perp$ mode, while in the experiment, it corresponds to an increased intensity of the lowest curve branch.

In the Type II spectra, as shown in Fig. 3(b) and (d), we can identify the same five transition points as for the Type I spectra, with a few distinctive features, which in the simulations appear more important than in the experiments, and occur as a result of mutual macrospin interaction. In fact, the simulations of both $F_\perp$ and $EM_\perp$ show slight differences, mostly due to the different configuration at the edges of the macrospins: in Type I each macrospin has non-equivalent edges (imbalance), in Type II each macrospin has equivalent edges (balance) with respect to the external field. However, the overall FMR behavior is quite similar to Type I. First, as outlined above, starting from +900 Oe, a liner (Larmor) frequency decrease, followed, below H_1, by a gradual frequency increase. Then, as shown in Fig. 6, the magnetization

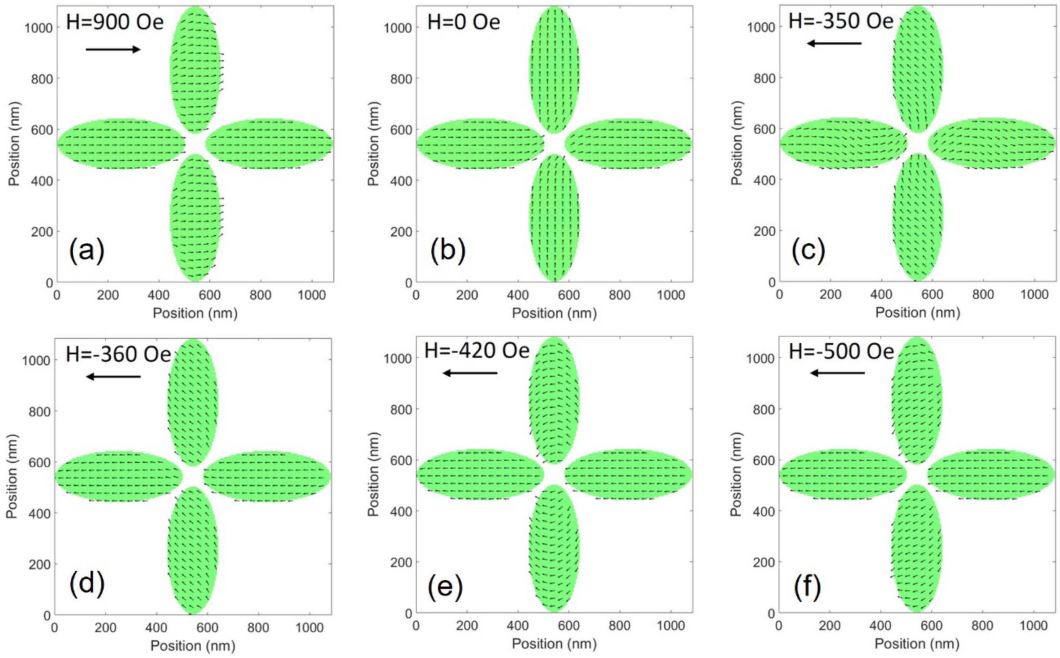

Fig. 5. (Color online) Micromagnetic simulation of the magnetization map of Type I at critical field values where FMR spectra show discontinuity. From H=900 Oe (a) through H=0 Oe (b) until H = –350 Oe (c), the magnetization in the macrospins perpendicular to the field gradually rotates counterclockwise; at $H_3 = -360$ Oe (d) macrospins parallel to the field undergo magnetization reversal; at $H_4 = -420$ Oe (e) the magnetization in the macrospins perpendicular to the field get a C-shape magnetization distribution, which gives a distinctive signature in the spectra; at $H_5 = -500$ Oe (f) the magnetization finally switches to a mirror configuration of the corresponding positive field values.

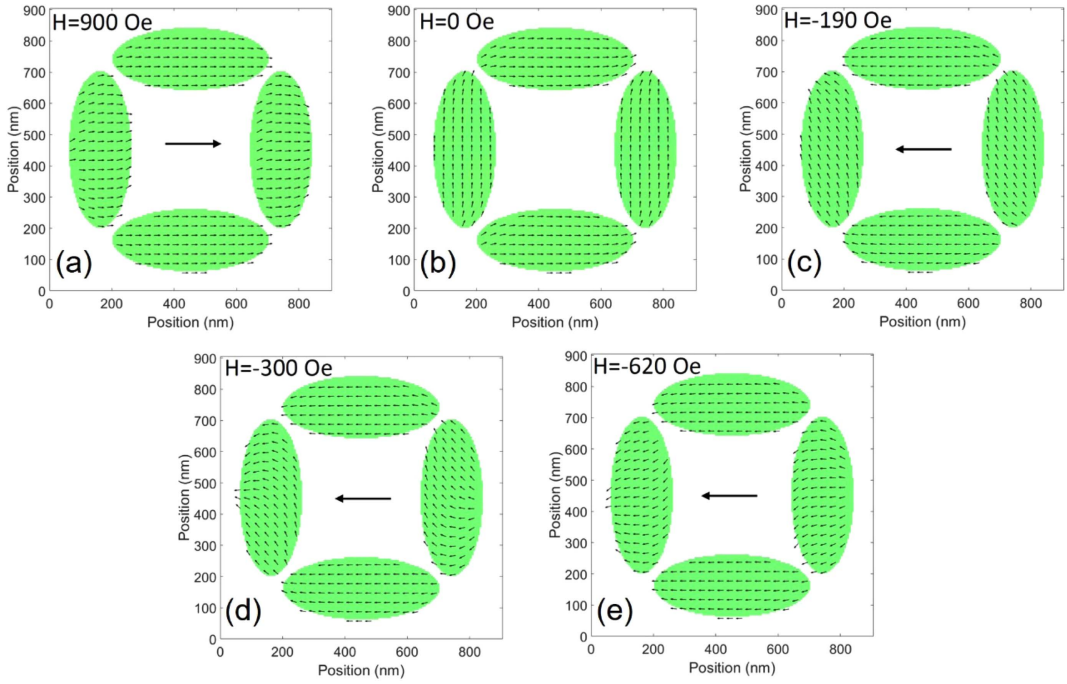

Fig. 6. (Color online) Micromagnetic simulation of the magnetization map of Type II at critical field values where FMR spectra show discontinuity. From H=900 Oe (a) through H=0 Oe (b) the magnetization of the macrospins perpendicular the applied field undergo a gradual rotation; at $H_3 = -190$ Oe (c) (–140 Oe in the experiment) the macrospins parallel to the applied field undergo a magnetization reversal, causing a strong frequency discontinuity in the FMR spectrum. Then, at $H_4 = -300$ Oe (d) the magnetization of the macrospins perpendicular to the applied field switch from an S-state to an (asymmetric) C-state: in this case, only modes localized in these macrospins show a likewise frequency discontinuity. Finally, at $H_5 = -620$ Oe (e), the system switches to a mirror configuration of the magnetization at corresponding positive applied field values.

reversal of the macrospins parallel to the applied field occurs at $H_3 = -190$ Oe (Type II has a less stable magnetization than Type I). At $H_4 = -300$ Oe the magnetization changes to a C-state (see also Fig. 6 for the corresponding magnetization maps), until $H_5 = -620$ Oe where the symmetry is recovered bringing the system to mirror state of the magnetization at positive field values.

In Fig. 7, we show the spectra of Type III and IV. In both types the orientation of the macrospins with respect to the applied field is the same (at 45°). Hence, the bulk modes of all four macrospins are almost degenerate in frequency (no more distinction between $F_{||}$ and $F_{\perp}$ or $EM_{||}$ and $EM_{\perp}$, see Fig. 4(g), (h) for Type III and (i), (j) for Type IV)), and so are the corresponding curves, as confirmed by both the experiments and the simulated spectra. In the simulation, we can see several curves almost parallel to that for the fundamental mode (F), which are higher order modes, with nodal lines perpendicular to the magnetization direction, referred to as "backward" (BA) modes. Only in the measured spectrum of Type IV is it possible to appreciate this feature, probably corresponding to the BA mode with 2 nodal lines (2-BA), which shows the largest intensity in the simulations. As a feature of the simulations shown in Fig. 4, the profiles of the F modes in Type III and IV are hybridized with the profile of higher order BA modes (see, for example, Ref. [22]). Micromagnetic simulation of the magnetization maps of Type III and IV at magnetized and reversal fields are shown in Fig. 8.

Another discussion concerns the edge modes (EM). We now consider the magnetization in the macrospins. While the magnetic charges at the macrospin edges in Type II (Type IV) occur only in couples, we found, at the same vertex, four alternate magnetic charges (2 in-2 out) in Type I (Type III): this condition strongly minimizes the dipolar interaction, which in turn favors a higher frequency [23, 24]. However, this aspect can be appreciated only in the simulations, since EM are notoriously vanishing in typical experimental FMR spectra, because their oscillation involves a small magnetization area.

In Type III and IV spectra, only a single transition is found, which is the magnetization reversal of all the four macrospins. The reversal is simultaneous for all the macrospins, since they are equivalently oriented with

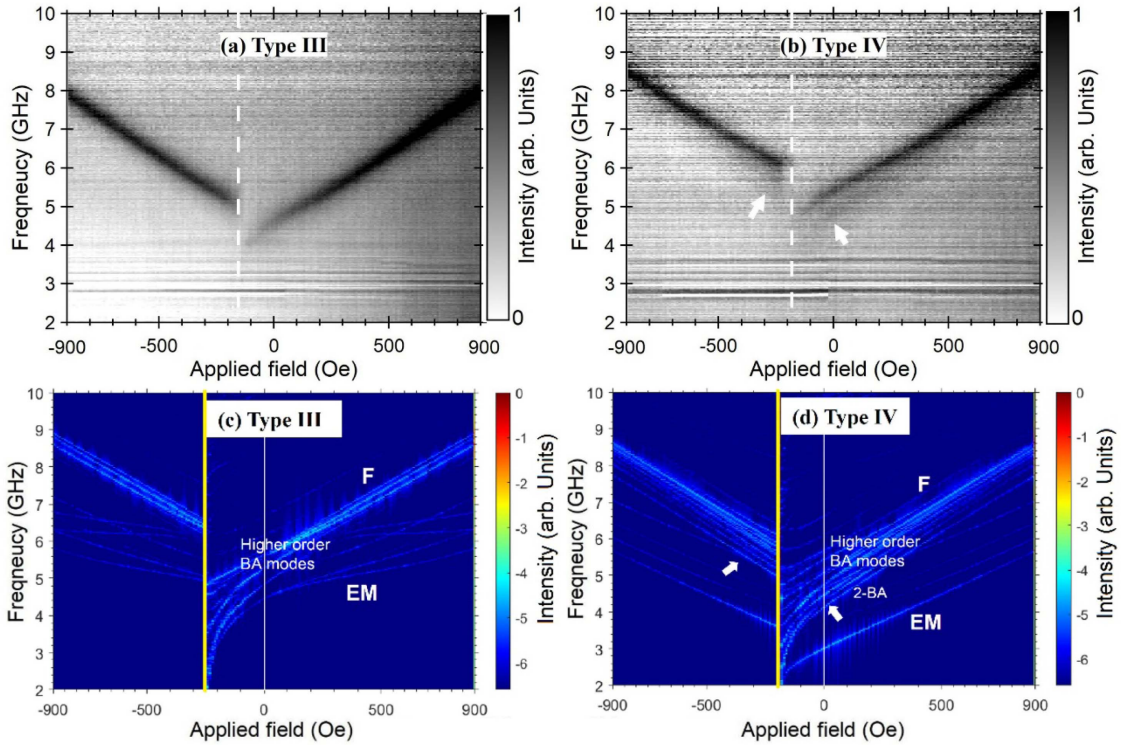

Fig. 7. (Color online) The experimental FMR spectra (top (a) and (b)) compared with theoretical simulations (bottom (c) and (d)) for Type III and Type IV macrospin structures. In these structures, the major axes of each macrospin is rotated 45 degrees from the applied magnetic field, as shown in Fig. 1. Just one transition is seen for these arrays, corresponding to the magnetization reversal of all the macrospins, occurring in the experiments (simulations) at H = –150 Oe (–250 Oe) for Type III, and H = –180 Oe (–220 Oe) for Type IV.

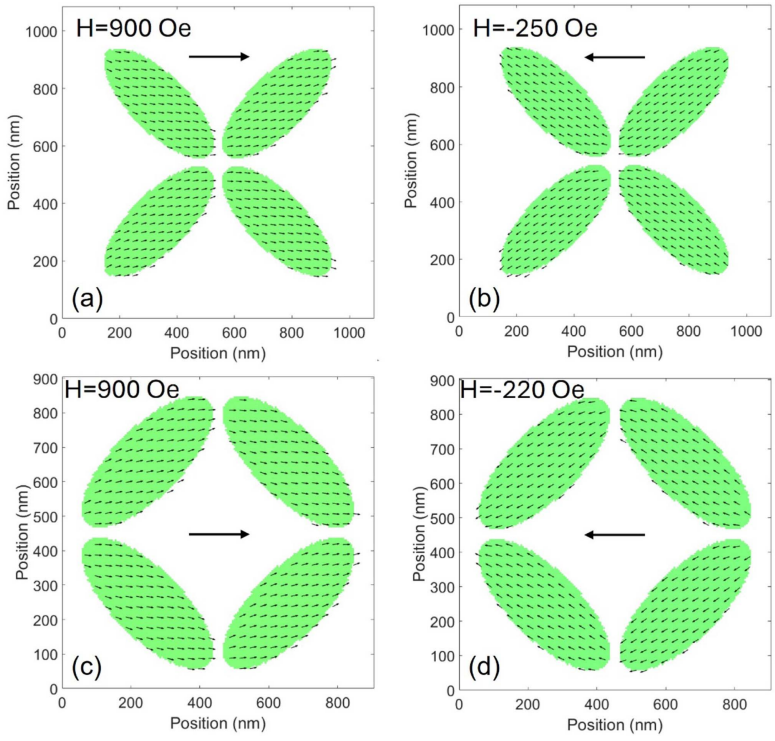

Fig. 8. (Color online) Micromagnetic simulation of the magnetization maps of Type III (a) and Type IV (c) systems at H=900 Oe, showing Type III (b) and Type IV (d) at the reversal fields, respectively.

respect to the applied field direction, as shown in Fig. 7. Again, due to the specific configuration of the macrospin edges, Type III is more stable than type IV, hence in simulations, the switching occurs at a slightly larger (negative) field magnitude of –250 Oe (–220 Oe for Type IV). In fact, in the experiment, the discontinuity is seen at about –150 Oe for Type III and around –180 Oe for Type IV, which seems to contradict Type III being more stable than Type IV. We suspect that this minor discrepancy is an indication of a smaller interaction between macrospins. A slightly larger macrospin separation in the fabricated Type IV clusters in Fig. 2(c)-(d) might be responsible for a reduction of the dipolar coupling and hence favor stability and a slightly larger (negative) reversal field. Furthermore, after the reversal, the measured FMR curve starts immediately for Type III, while at H = –210 Oe for Type IV.

Finally, we would like to remark once more how, with reference to the simulations, the different configuration of the macrospin edges causes significantly different simulated reversal fields of the macrospins parallel to the applied field: –360 Oe for Type I (more stable configuration), –190 for Type II (less stable configuration). In Type III and IV, all macrospins switch almost simultaneously at –250 Oe for Type III, and –220 Oe for Type IV. When comparing the reversal fields of the four Types in relation to the stability of the cluster, we should refer only to the field at which the magnetization has a negative component in all macrospins. Based on the simulation results, we find H_3 = –360 Oe (Type I), H_3 = –190 Oe (Type II), H= –250 Oe (Type III), and H = –220 Oe (Type IV). This means that Type II appears to be the softer configuration, with a magnetization which can be easily curled and reversed. Second, but not less important, the different macrospin configuration has an impact on the dynamics: simulations show that modes $F_\perp$ and $EM_\perp$ of Type I and Type II behave quite differently. For example, in Type I, the FMR curve of $F_\perp$ intersects the curve of $EM_\perp$ only when H<300 Oe; in contrast, in Type II, the $F_\perp$ and $EM_\perp$ curves intersect already at H=500 Oe, with a distinctive anticrossing mark (a gap is formed). This is a form of magnon-magnon interaction [10], which strictly dependents on the distance between macrospins, and is, hence, adjustable by modifying the geometry. While interesting, this complex effect is outside the scope of the present paper.

4. Conclusions

In conclusion, we have conducted both experimental and theoretical studies of spin wave modes in four distinct types of macrospin arrays. In moving from Type I-II to Type III-IV, we observed two key effects: a reduction from two to a single dominant spin wave resonance and a decrease in its corresponding frequency. Additionally, a subtle yet measurable effect appears in the spectra: whereas the edge mode curves are faintly visible in Type I-II, they are completely absent in Type III-IV. Finally, the spectra show a dependence both of the discontinuity of the FMR curves (associated with different magnetization reversal fields) and a form of magnon-magnon interaction due to the underlying macrospin configuration. These findings enhance our understanding of spin wave dynamics in macrospin systems and provide insights for future studies on engineered magnetic systems including magnon-magnon hybrid systems.

Acknowledgements

Work at Korea University of Technology and Education was supported by the Education and Research Promotion Program of KOREATECH in 2023 and the National Research Foundation of Korea (NRF) grant funded by the Korea government (MSIT) (No. 2021R1G1A1092937). Work at Delaware is based upon work supported by the National Science Foundation under Grant No. 2339475. Work at Northwestern involving experimental design and FMR measurements and manuscript preparation was supported under NSF Grant DMR 1507058. Work at University of Ferrara was supported by the Department of Physics and Earth Sciences Grant Bando FIRD 2024, and the CINECA award under the ISCRA initiative, for the availability of high-performance computing resources and support.

References

[1] L. J. Heyderman and R. L. Stamps, J. Phys. Condens. Mat. **25**, 363201 (2013).
[2] R. Negrello, F. Montoncello, M. T. Kaffash, M. B. Jungfleisch, and G. Gubbiotti, APL Mater. **10**, 091115 (2022).
[3] S. H. Skjærvo, C. H. Marrows, R. L. Stamps, and L. J. Heyderman, Nat. Rev. Phys. **2**, 13 (2020).
[4] R. F. Wang, C. Nisoli, R. S. Freitas, J. Li, W. McConville, B. J. Cooley, M. S. Lund, N. Samarth, C. Leighton, V. H. Crespi, and P. Schiffer, Nature. **439**, 303 (2006).
[5] M. Krawczyk and D. Grundler, J. Phys. Condens. Mat. **26**, 123202 (2014).
[6] J. C. Gartside, K. D. Stenning, A. Vanstone, H. H. Holder, D. M. Arroo, T. Dion, F. Caravelli, H. Kurebayashi, and W. R. Branford, Nat. Nanotechnol. **17**, 460 (2022).
[7] P. Gypens, J. Leliaert, and B. Van Waeyenberge, Phys.

Rev. Appl. **9**, 034004 (2018).
[8] J. Drisko, T. Marsh, and J. Cumings, Nat. Commun. **8**, 14009 (2017).
[9] V. S. Bhat and M. B. Jungfleisch, Appl. Phys. Lett. **126**, 022406 (2025).
[10] T. Dion, K. D. Stenning, A. Vanstone, H. H. Holder, R. Sultana, G. Alatteili, V. Martinez, M. T. Kaffash, T. Kimura, R. F. Oulton, W. R. Branford, H. Kurebayashi, E. Iacocca, M. B. Jungfleisch, and J. C. Gartside, Nat. Commun. **15**, 4077 (2024).
[11] A. Frotanpour, J. Woods, B. Farmer, A. P. Kaphle, L. E. De Long, L. Giovannini, and F. Montoncello, Phys. Rev. B. **102**, 224435 (2020).
[12] A. Frotanpour, J. Woods, B. Farmer, A. P. Kaphle, J. T. Hastings, and L. E. DeLong, Phys. Rev. B. **103**, 184402 (2021).
[13] P. Micaletti and F. Montoncello, Magnetochemistry. **9**, 158 (2023).
[14] C. H. Marrows, J. Barker, T. A. Moore, and T. Moorsom, npj Spintronics. **2**, 12 (2024).
[15] W. Bang, J. Sturm, R. Silvani, M. T. Kaffash, A. Hoffmann, J. B. Ketterson, F. Montoncello, and M. B. Jungfleisch, Phys. Rev. Appl. **14**, 014079 (2020).
[16] M. B. Jungfleisch, W. Zhang, E. Iacocca, J. Sklenar, J. Ding, W. Jiang, S. Zhang, J. E. Pearson, V. Novosad, J. B. Ketterson, O. Heinonen, and A. Hoffmann, Phys. Rev. B. **93**, 100401(R) (2016).
[17] F. Montoncello, L. Giovannini, W. Bang, J. B. Ketterson, M. B. Jungfleisch, A. Hoffmann, B. W. Farmer, and L. E. De Long, Phys. Rev. B. **97**, 014421 (2018).
[18] W. Bang, F. Montoncello, M. T. Kaffash, A. Hoffmann, J. B. Ketterson, and M. B. Jungfleisch, J. Appl. Phys. **126**, 203902 (2019).
[19] W. Bang, M. T. Kaffash, M. T. Hossain, A. Hoffmann, J. B. Ketterson, and M. B. Jungfleisch, AIP Adv. **12**, 035131 (2022).
[20] A. Vansteenkiste, J. Leliaert, M. Dvornik, M. Helsen, F. Garcia-Sanchez, and B. Van Waeyenberge, AIP Adv. **4**, 107133 (2014).
[21] J. Chang, V. L. Mironov, B. A. Gribkov, A. A. Fraerman, S. A. Gusev, and S. N. Vdovichev, J. Appl. Phys. **100**, 104304 (2006).
[22] A. Gubbiotti, L. L. Xiong, F. Montoncello, L. Giovannini, and A. O. Adeyeye, J. Appl. Phys. **124**, 083903 (2018).
[23] D. Kuzma, F. Montoncello, P. Sobieszczyk, A. Wal, L. Giovannini, and P. Zielinski, J. Appl. Phys. **124**, 223902 (2018).
[24] M. J. Morrison, T. R. Nelson, and C. Nisoli, New J. Phys. **15**, 045009 (2013).